PAPER • OPEN ACCESS

Unlocking photon–magnon interplay via saturation magnetization

IOP Publishing New J. Phys. 27 (2025) 104506 https://doi.org/10.1088/1367-2630/ae0ea8

New Journal of Physics
The open access journal at the forefront of physics

Deutsche Physikalische Gesellschaft DPG
IOP Institute of Physics

Published in partnership with: Deutsche Physikalische Gesellschaft and the Institute of Physics

PAPER

Unlocking photon–magnon interplay via saturation magnetization

Sachin Verma[1], **Jiten Mahalik**[2], **Abhishek Maurya**[1], **Rajeev Singh**[1] and **Biswanath Bhoi**[1,*]

[1] Nano-Magnetism and Quantum Technology Lab, Department of Physics, Indian Institute of Technology (Banaras Hindu University) Varanasi, Varanasi 221005, India
[2] National Institute of Science Education and Research, Bhubaneswar, Odisha, India
[*] Author to whom any correspondence should be addressed.

E-mail: biswanath.phy@itbhu.ac.in and sachinverma.rs.phy22@iitbhu.ac.in

Keywords: hexagonal ring resonator (HRR), hybrid quantum system, saturation magnetization, quantum information processing

Supplementary material for this article is available online

OPEN ACCESS

RECEIVED
5 June 2025

REVISED
1 September 2025

ACCEPTED FOR PUBLICATION
2 October 2025

PUBLISHED
16 October 2025

Abstract

Photon–magnon hybrid systems present a promising platform for the development of next-generation devices in quantum information processing and quantum sensing technologies. In this study, we investigate the control of photon–magnon coupling (PMC) strength through systematic variation of the saturation magnetization (M_s) in a planar hexagonal-ring resonator integrated with a yttrium iron garnet (YIG) thin film configuration. Using full-wave numerical simulations in CST Microwave Studio, we demonstrate that tuning the M_s of the YIG film from 175 mT to 90 mT enables systematic control over the coupling strength across the 127–51 MHz range at room temperature. To explain the observed PMC dynamics, we develop a semiclassical analytical model based on electromagnetic theory, that accurately reproduces the observed coupling behavior, revealing the key role of spin density in mediating the light–matter interaction. The model is further extended to include the effects of variable magnon damping across different M_s values, enabling broader frequency control. These findings establish M_s as a key tuning parameter for tailoring PMC, with direct implications for the design of tunable hybrid systems for reconfigurable quantum devices.

1. Introduction

Hybrid quantum systems (HQSs) have emerged as a versatile platform where distinct physical excitations such as photons, magnons, phonons, plasmons, electrons, and even thermal quasiparticles are coupled to harness their complementary advantages while overcoming the limitations inherent to individual subsystems [1–6]. By enabling controlled interactions among these diverse quantum degrees of freedom, HQS provides a powerful framework for developing next-generation quantum technologies. These include high-precision quantum sensors [7, 8], coherent quantum transducers [9] for interfacing different frequency domains, robust quantum memories [10], and scalable architectures for quantum information processing [11] and communication.

Among the various types of HQSs, photon–magnon coupled (PMC) platforms where microwave photons coherently interact with magnons have attracted significant attention [2]. By combining the long coherence times and magnetic tunability of magnons with the high-speed, low-loss transmission capabilities of photons, these systems offer a promising route toward quantum signal processing, memory, and transduction applications [5]. In recent years, PMC systems have achieved remarkable progress [2], extending beyond strong coupling and coherent information exchange to enable the observation of exotic phenomena such as level attraction [12], non-reciprocal behavior [13], and various aspects of non-Hermitian physics [14, 15], including exceptional points [16, 17] and, more recently, exceptional surfaces [18]. Realizing a broad range of such exotic phenomena in HQS critically depends on the ability to precisely control PMC. Several strategies have been developed to modulate the coupling strength, such as engineering the geometry [19] and mode volume of microwave resonators [20], and dynamically tuning the relative detuning between photon and magnon modes through external magnetic

fields [21]. Furthermore, the spatial positioning and orientation of the magnetic material within the resonator's field profile provide additional fine-tuning of the coupling rate [22, 23]. These control techniques underscore the pivotal role of PMC tunability in advancing both the fundamental understanding and technological applications of HQSs.

Despite significant progress in controlling PMC strength, existing methods face inherent limitations. Geometric modifications of resonators and spatial repositioning of magnetic elements offer only static or limited tunability, often requiring complex fabrication or mechanical adjustments. Frequency detuning through external magnetic fields, while widely used, affects both the magnon and photon modes simultaneously, making it difficult to isolate the effect on coupling strength alone. Moreover, dynamic modulation approaches involving parametric drives or nonlinear interactions introduce added complexity and may compromise coherence. In this context, one often overlooked yet fundamentally promising avenue is the direct tuning of the saturation magnetization (M_s) of the magnetic material itself. Since the coupling strength scales with the square root of spin density [2, 5], altering M_s directly modifies the number of spins available for interaction, providing a clean and intrinsic means of tuning PMC without perturbing resonator geometry or mode structure.

Motivated by these considerations, we propose and investigate a strategy centered on magnetic saturation tuning as a direct and versatile control knob for PMC. In this work, we explore a novel approach for controlling the strength of PMC by systematically varying the M_s of the magnetic system, which excites magnons to hybridize with photons generated by a microwave resonator. Using full-wave numerical simulations in CST Microwave Studio, we demonstrate that tuning M_s enables a wide and systematic control of the coupling strength range at room temperature. To further understand the PMC dynamics, we develop a semiclassical analytical model based on electromagnetic theory, which accurately reproduces the observed behavior and highlights the key role of spin density in mediating light–matter interactions. By incorporating magnon damping variations with M_s, the model extends the tunability across a wider frequency range. These findings establish M_s as an effective tuning parameter for engineering PMC, offering new opportunities for the development of reconfigurable HQSs and devices.

2. Numerical modeling and simulation setup

Figure 1 presents the schematic of the photon–magnon hybrid system, illustrating the simulation setup comprising a yttrium iron garnet (YIG) thin film coupled to a hexagonal-ring resonator (HRR) via a microstrip transmission line in a planar geometry.

The HRR is employed here as it offers a superior balance of field localization and symmetry compared to circular or square rings. Its geometry ensures stronger confinement of the microwave magnetic field within the trackwidth region, maximizing overlap with the YIG film and enabling robust photon–magnon coupling [24]. In addition, the compact design supports higher miniaturization and stronger magnetic coupling, while the symmetric structure enhances mode control and suppresses unwanted splitting. Together, these features yield significantly improved Q-factors, making the HRR an optimal platform for the proposed hybrid system [25].

In this configuration, the HRR supports the photon mode, while the YIG film serves as the medium for magnon excitation. To investigate their interaction, full-wave electromagnetic simulations were performed using CST Microwave Studio. The microstrip transmission line was placed on the front side of the sample to efficiently excite both the HRR and the YIG film, with a continuous ground plane positioned on the back side. When an alternating current at microwave frequencies is driven through the microstrip, it generates a localized microwave magnetic field around the microstripline and an electric field that terminates perpendicularly onto the ground plane. The microwave magnetic field excites the HRR, which acts as a parallel LC resonator, exhibiting a quasi-static photon mode at its resonant frequency. To enable magnon excitation, a uniform in-plane external bias magnetic field (H) was applied across the YIG film, tuning the magnon resonance frequency by aligning the magnetization and enabling coherent, uniform spin precession at the desired frequency [23]. YIG was selected due to its high spin density and exceptionally low magnetic damping, making it an ideal material for coherent information processing applications.

The material and geometric parameters used in the simulations are as follows. For the YIG film, the gyromagnetic ratio is $\gamma = 1.76 \times 10^7$ rad Oe^{-1}, the saturation magnetization is $\mu_0 M_{sat} = M_s = 172$ mT, the damping constant is $\alpha = 1.4 \times 10^{-4}$, and the magnetic anisotropy constant is taken to be zero. The HRR is patterned on a dielectric substrate of dimensions 30 mm $\times$ 20 mm $\times$ 0.64 mm, with dielectric constant 10.2 and a dissipation factor of 0.0012 at 10 GHz. A microstrip line is placed close to the HRR, designed with a width $w = 0.57$ mm, length $l = 30$ mm, and thickness $t = 35\,\mu$m to achieve a characteristic impedance of 50 Ω, while a YIG film of size 3 mm $\times$ 3 mm $\times$ 20 μm was placed at the edge of the

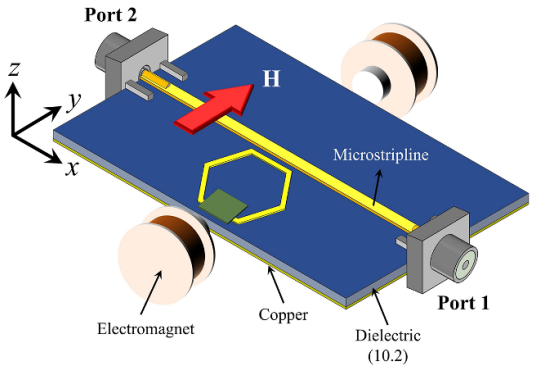

Figure 1. Schematic representation of the simulation setup for a magnon–photon hybrid system comprising a YIG film (green), a microstrip line (dark yellow), a dielectric material (navy blue), and an HRR (dark yellow). The YIG film is positioned at the edge of the HRR, which is placed adjacent to the microstrip line. An external magnetic field (H) is applied uniformly in-plane along the y-axis.

HRR (dimensions: outer radius = 4 mm, inner radius = 3.4 mm) to maximize photon–magnon interaction. We simulated for the transmission spectra $|S_{21}|$ as a function of the frequency of the microwave current in the presence of a static external magnetic field (H) applied along the y-direction [23]. The $|S_{21}|$, denotes the forward scattering parameter of the microwave network, defined as the ratio of the transmitted signal at port 2 to the input at port 1. Physically, $|S_{21}|$ represents the fraction of microwave power transmitted through the HRR-YIG system, where it's resonant features directly reflect photon-magnon hybridization. Hence, variations in $|S_{21}|$ provide a sensitive measure of the coupling strength and the formation of hybrid modes in the proposed device.

3. Results and discussion

To investigate dynamic interaction between photon and magnon, the transmission characteristics $|S_{21}|$ was analyzed by systematically varying the strength of H applied along the y-axis. This method allowed for the examination of both the individual responses of the HRR and the YIG film, as well as their collective behavior in the hybrid configuration. The photon mode resonance frequency of the HRR was identified at $\frac{\omega_c}{2\pi} = 5.33$ GHz and remained invariant with respect to changes in the applied magnetic field. This field-independence arises because the resonance frequency, given by $\omega_c = 1/\sqrt{LC}$, is determined solely by the resonator's inductance and capacitance, and is unaffected by external magnetic fields. The damping factor of the HRR was calculated as $\beta = \frac{\Delta\omega_c}{\omega_c} = 4.69 \times 10^{-3}$, where $\Delta\omega_c$ denotes the half-width at half-maximum of the $|S_{21}|$ response. These parameters were extracted from numerical simulations conducted on the HRR structure alone, without the inclusion of the YIG film. In contrast, the resonance frequency of the YIG film displayed a strong dependence on the applied magnetic field, shifting to higher frequencies as the field strength increased. This behavior, observed through simulations performed solely on the YIG film, follows the Kittel relation: $\omega_r = \gamma\sqrt{H(H+M_s)}$.

In the HRR–YIG hybrid system, two distinct resonance peaks were observed. The photon mode peak associated with the HRR remained nearly constant throughout the H sweep, while the magnon mode peak corresponding to the YIG film shifted progressively to higher frequencies with increasing magnetic field. As the magnon mode approached the photon mode frequency, an increase in its amplitude was observed. After crossing the photon mode, the amplitude of the magnon mode gradually decreases (See figure S1 in supplementary file). This characteristic evolution indicates strong coupling between the photon mode of the HRR and the magnon mode of the YIG film.

3.1. Effect of magnetization on photon–magnon interactions

To investigate the influence of M_s on the photon–magnon interaction and its effect on coupling strength in the HRR–YIG hybrid system, we conducted a series of simulations for various M_s values of the YIG thin film, specifically 175 mT, 150 mT, 120 mT, and 90 mT. All other material and geometrical parameters of the YIG film and HRR were kept constant. Figures 2(a)–(d) present the transmission spectra $|S_{21}|$ as a function of f and H for the different M_s values. The colormap background in each plot represents the simulation data, illustrating the photon–magnon hybridization in the system.

We begin the discussion of the simulation results with the case of $M_s = 175$ mT, as shown in figure 2(a). In this case, when the magnon mode frequency is tuned to resonance with the microwave

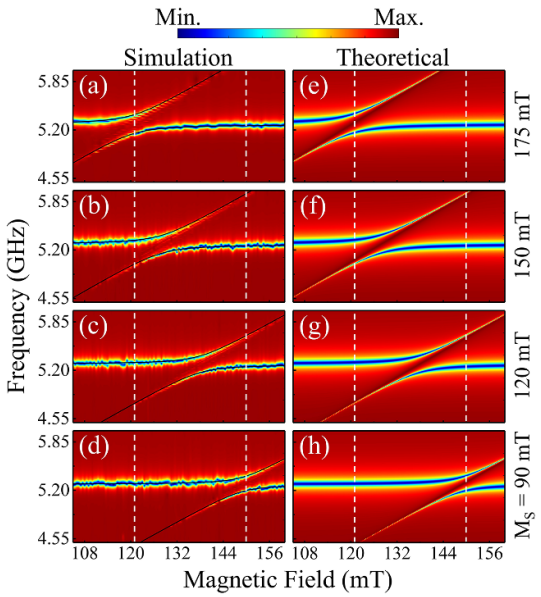

Figure 2. Scanned $[f, H]$ dispersion of microwave $|S_{21}|$ power plotted for different saturation magnetization (M_s) values: (a)–(d) simulation results, and (e)–(h) theoretical calculations based on an electrodynamic model. The white lines indicate the shift of the coupling center as M_s decreases from 175 mT to 90 mT.

photon mode, a characteristic normal-mode anti-crossing is observed. This phenomenon, indicative of coherent coupling between the photon and magnon modes, occurs at the coupling center, located at $H_{cent} = 121$ mT. The normal-mode anti-crossing behavior, indicating strong coupling, is similarly observed for the other M_s values of 150 mT, 120 mT, and 90 mT, as seen in figures 2(b)–(d). However, a clear trend emerges upon examining the coupling centers across the different M_s values. Specifically, the coupling centers H_{cent} for $M_s = 150$ mT, 120 mT, and 90 mT shift to higher magnetic fields, with values of 128.5 mT, 138.5 mT, and 150 mT, respectively. On the other hand, the splitting between the hybridized modes is observed to decrease monotonically as the M_s decreases from 175 mT to 90 mT. This shift of the coupling center to higher magnetic fields, accompanied by a reduction in mode splitting, is a direct consequence of the decrease in M_s, further emphasizing the tunability of the photon–magnon interaction through variations in the saturation magnetization. To emphasize this trend, vertical white lines are used to mark the coupling centers for $M_s = 175$ mT and $M_s = 90$ mT, clearly illustrating the total shift of 29 mT in the magnetic field. These results suggest that the strength and characteristics of the PMC in the hybrid system can be systematically controlled by varying the M_s of the magnetic system, providing a valuable mechanism for tuning the interaction in potential quantum devices.

To gain deeper insight into the observed behavior of the PMC and to quantitatively describe the dependence of the hybridized mode characteristics on the saturation magnetization, a theoretical model is essential. By establishing a suitable theoretical framework, we can better understand the underlying physical mechanisms governing the coupling strength, observed shifts in coupling center, and mode splitting. In the following section, we present the theoretical modeling of the HRR–YIG hybrid system, which captures the essential features observed in the simulations and provides a quantitative basis for further analysis.

3.2. Theoretical formalism

The photon–magnon interactions in hybrid systems are effectively described by a semiclassical framework that combines the microwave LCR circuit model with the Landau–Lifshitz–Gilbert (LLG) dynamics. These interactions originate from two classical coupling mechanisms. The first, Faraday induction [26], induces a voltage in the LCR circuit due to the precession of the magnetization. The second, based on Ampère's law [27], involves magnetic fields generated by the circuit's current, which in turn affect the magnetization. Let's consider a microwave current $j_0^+ = j_0 e^{-i\omega t}$ flowing through the microstrip line. According to Ampère's law, this current generates a microwave magnetic field $h_{line} = h e^{-i\omega t}$ around the microstripline, characterized by an amplitude $|h|$ and an angular frequency ω, and the magnetization corresponding to the magnon is given by $\mathbf{m}^+ = \mathbf{m} e^{-i\omega t}$.

The magnetization precession in the YIG film is described by the LLG equation [28, 29],

$$\frac{\mathrm{d}\mathbf{m}}{\mathrm{d}t} = -\gamma\,\mathbf{m}\times\mathbf{H}_{\mathrm{eff}} + \alpha\,\mathbf{m}\times\frac{\mathrm{d}\mathbf{m}}{\mathrm{d}t} \tag{1}$$

where $\mathbf{m} = \mathbf{M}/M_s$ represents the magnetization vector, with gyromagnetic ratio $\gamma/2\pi$, intrinsic Gilbert damping parameter α, and saturation magnetization M_s of the YIG film. $\mathbf{H}_{\mathrm{eff}}$ is the effective magnetic field on the YIG film as $\mathbf{H}_{\mathrm{eff}} = H_{\mathrm{dc}} + \mathbf{h}_{\mathrm{line}} + \mathbf{h}_{\mathrm{HRR}} = H\hat{\mathbf{y}} + \mathbf{h}e^{-i\omega t}$, where H_{dc} is the externally applied DC magnetic field along the y-axis. The magnetizations in the YIG are influenced by the effective field $\mathbf{h}e^{-i\omega t}$, which is the sum of two time-dependent magnetic fields $\mathbf{h}_{\mathrm{line}}$ from the feeding line and $\mathbf{h}_{\mathrm{HRR}}$ due to the $\mathbf{j}^+$. Using a linearized form of the magnetization direction, the magnetization variation is given as, $\mathbf{m} = M_s\hat{\mathbf{y}} + \mathbf{m}^+$, where $\mathbf{m}^+$ is the oscillating component of the magnetization and M_s is the magnetization along the z direction. Assuming $|\mathbf{m}^+| \ll M_s$, the LLG equation can be simplified in the rotational frame [27, 30] as,

$$(\omega - \omega_r + i\alpha\omega)\,m^+(t) - i\omega_m K_A j^+(t) = 0 \tag{2}$$

where $m^+ = m_x + i m_y$, represents the in-plane magnetization for the magnon mode, $\omega_m = \gamma M_{\mathrm{s}}$ [30, 31]. The ferromagnetic resonance (FMR) frequency is given by $\omega_r = \gamma\sqrt{H(H+M_s)}$, and $j^+ = i(h^+)_{\mathrm{HRR}}K_A$, is the net microwave current in the HRR, and K_A is the coupling parameter that determines the phase relation between the HRR's photon and YIG's magnon modes due to Ampere's law.

As there is a microwave current j_0^+ flowing through the microstrip line, it induces a voltage of $V_1 = L\frac{\mathrm{d}j_0^+}{\mathrm{d}t}$ in the HRR, and due to the presession of spins of YIG an additional driving voltage $V_2 = iK_F L\frac{\mathrm{d}m^+}{\mathrm{d}t}$, is also induced in the HRR according to the Faraday induction law. Where K_{F} is the coupling parameter to account for the phase relation between the HRR's photon mode and YIG's magnon mode. This induced voltage $V^+ = L\frac{\mathrm{d}j_0^+}{\mathrm{d}t} + iK_F L\frac{\mathrm{d}m^+}{\mathrm{d}t}$, generates a microwave current in the HRR, as expressed by $V^+ = Z_{\mathrm{HRR}}j^+$, where Z_{HRR} being the resonator's impedance and j^+ is the net current in the HRR. Now, according to an equivalent LCR circuit model [31–33],

$$V^+ = Rj^+ + \frac{1}{C}\int j^+\,\mathrm{d}t + L\frac{\mathrm{d}j^+}{\mathrm{d}t} \tag{3}$$

where, R, C, and L represent the resistance, capacitance, and inductance, respectively. By solving the above equation, we get,

$$\left(\omega^2 - {\omega_c}^2 + 2i\beta\omega\omega_c\right)j^+(t) + i\omega^2 K_F m^+(t) = \omega^2 {j_0}^+ \tag{4}$$

where, $\omega_{\mathrm{c}} = 1/\sqrt{LC}$ is the angular resonance frequency of the HRR with $\beta = R/(2L\omega_c)$, where β is the damping parameter with resistance R. To simultaneously solve equations (2) and (4), the matrix form is reformulated as:

$$\begin{bmatrix} \omega^2 - {\omega_c}^2 + 2i\beta\omega\omega_c & i\omega^2 K_F \\ -i\omega_m K_A & \omega - \omega_r + i\alpha\omega \end{bmatrix}\begin{bmatrix} j^+ \\ m^+ \end{bmatrix} = \begin{bmatrix} \omega^2 {j_0}^+ \\ 0 \end{bmatrix}. \tag{5}$$

Let,

$$\Omega = \begin{bmatrix} \omega^2 - {\omega_c}^2 + 2i\beta\omega\omega_c & i\omega^2 K_F \\ -i\omega_m K_A & \omega - \omega_r + i\alpha\omega \end{bmatrix}. \tag{6}$$

Now, equation (5) can be written as,

$$\Omega\begin{bmatrix} j^+ \\ m^+ \end{bmatrix} = \begin{bmatrix} \omega^2 {j_0}^+ \\ 0 \end{bmatrix}. \tag{7}$$

The first row of the matrix in equation (5) represents the coupling of the magnetization dynamics in the YIG film to the currents in the resonator, describing the LCR circuit influenced by the motion of magnetizations. Conversely, the second row of the matrix captures the influence of the net resonator currents on the magnetization dynamics within the YIG film. The solution of $\det(\Omega) = 0$ yields the complex frequency, where its real part corresponds to the dispersion spectrum, and its imaginary part reflects the dissipation in HRR-YIG hybrid system. To understand the observed dispersion spectra, we solve $\det(\Omega) = 0$, which gives:

$$\left(\omega^2 - {\omega_c}^2 + 2i\beta\omega\omega_c\right)(\omega - \omega_r + i\alpha\omega) - \left(\omega^2 K_F\right)(\omega_m K_A) = 0 \tag{8}$$

under the resonance condition, where $\omega_c = \omega_r$, above equation can be written as,

$$\tilde{\omega}_{\pm} = \frac{1}{2}\left[(\tilde{\omega}_r + \tilde{\omega}_c) \pm \sqrt{(\tilde{\omega}_r - \tilde{\omega}_c)^2 + 2K^2\omega_m\omega_c}\right] \tag{9}$$

here, $\tilde{\omega}_c = \omega_c - i\beta\omega_c$, $\tilde{\omega}_r = \omega_r - i\alpha\omega_r$, and $K^2 \cong K_A K_F$, where β and α denote the intrinsic damping rates of the photon and magnon modes, respectively. We have calculated the complex eigenvalues of two coupled modes expressed as $\tilde{\omega}_{\pm} = \omega_{\pm} - i\Gamma_{\pm}$ [27, 30, 34]. Here the $\omega_{\pm}$ represents the real part, corresponding to the higher and lower energy modes in the dispersion curve, while $\Gamma_{\pm}$ is the imaginary part, which describes the linewidth evolution of the coupled modes. The frequency gap between the two modes at the anti-crossing center is given by $(\omega_+ - \omega_-)/2\pi$, which can be determined from equation (9). The net coupling strength is defined as $\Delta = (\omega_+ - \omega_-)/4\pi$ representing half of the frequency gap between the upper and lower branches at the resonance point, where $\omega_c = \omega_r$. So, Δ can be expressed as,

$$\Delta = \frac{\omega_c}{4\pi}\sqrt{\frac{2K^2\gamma M_s}{\omega_c} - (\beta - \alpha)^2}. \tag{10}$$

To determine the coupling strengths, equation (9) was fitted to the lower- and higher-frequency branches as indicated by the black solid lines in figures 2(a)–(d). The simulation results are in agreement with the fitted curves, confirming the accuracy of the theoretical model. The resulting values of Δ were 127.6 MHz, 121.4 MHz, 113 MHz, and 97.68 MHz, corresponding to saturation magnetizations (M_s) values of 175 mT, 150 mT, 120 mT, and 90 mT, respectively. This decreasing trend in coupling strength with decreasing M_s can be understood by considering the fundamental dependence of PMC on the magnetization of the system. In magnetic materials like YIG, when all net spins precess coherently in phase, the collective excitation known as the Kittel mode couples strongly to the HRR cavity mode. In this regime, the coupling strength Δ scales with the square root of the total number of spins involved, i.e. $\Delta \propto \sqrt{N}$ [2, 5]. The saturation magnetization (M_s), which represents the maximum magnetization when all spins are aligned, is directly proportional to the spin density via the relation $M_s \propto Ng_s\mu_B/V$, where N/V is the spin density (number of spins per unit volume), g_s is the Lande g-factor, and μ_B is the Bohr magneton [35, 36]. Combining these relations yields $\Delta \propto \sqrt{M_s}$, indicating that the coupling strength is fundamentally linked to the square root of the saturation magnetization. These findings underscore the importance of maintaining high magnetic order and coherence to realize strong PMC.

To further validate the transmission characteristics of the coupled resonator–YIG system, the transmission coefficient $|S_{21}|$ was computed and plotted for the same values of M_s using an analytical expression derived from equation (7) within the framework of input-output theory [37], expressed as:

$$S_{21} = \Gamma\frac{j^+}{j_0^+} = \Gamma\frac{\omega^2(\omega - \omega_r + i\alpha\omega)}{det(\Omega)} \tag{11}$$

where, Γ is the normalized parameter. Figures 2(e)–(h) show the calculated $|S_{21}|$ spectra mapped over the $f - H$ plane by using equation (11). As M_s decreases, the coupling center shifts clearly toward higher magnetic fields in the theoretical results, consistent with the simulation data. This shift arises from the behavior of the magnon resonance frequency, which follows the Kittel equation: $\omega_r = \gamma\sqrt{H(H + M_s)}$. A reduction in M_s lowers the magnon resonance frequency. Since the HRR photon mode operates at a fixed frequency of 5.33 GHz, resonance requires the magnon mode to match this frequency. To compensate for the reduced magnon frequency due to a lower M_s, a higher external magnetic field is required to bring the magnon mode back into resonance with the photon mode. This explains the observed shift of the coupling center toward higher magnetic fields with decreasing magnetization. The strong agreement between theoretical predictions and simulation results further validates the model.

3.3. Effect of damping on photon–magnon interactions

Previous studies on PMC hybrid systems have demonstrated that damping plays a critical role in shaping the anticrossing dispersion and can significantly alter the observed coupling strength [34, 38, 39]. In broader contexts such as non-Hermitian and optomechanical systems, it has been shown that the nature of the eigenvalue dispersion whether it exhibits anticrossing or level attraction (i.e. crossing behavior) can depend on the imbalance in dissipation rates between the two interacting subsystems, even for a given coupling strength [40].

To systematically explore the influence of magnon damping on the PMC behavior in a strongly coupled system, we extended our CST microwave simulations by varying both the M_s and the α of

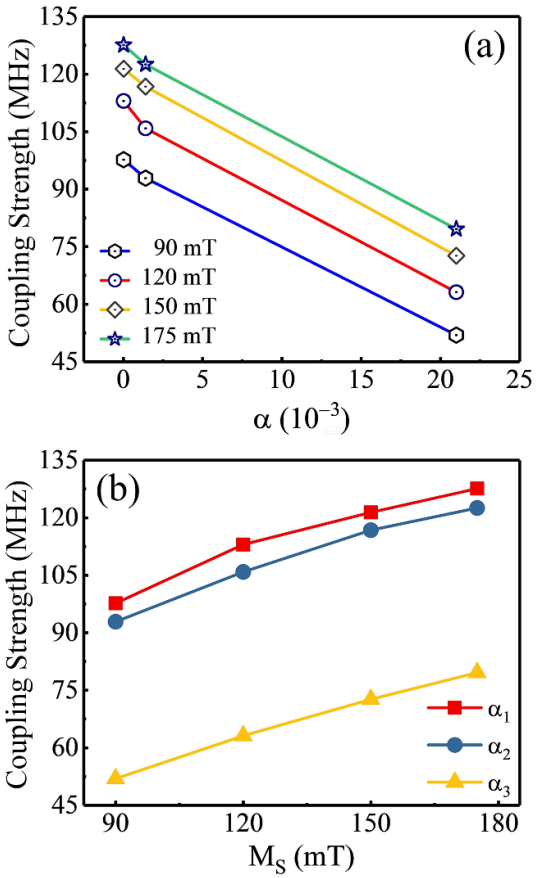

Figure 3. Coupling strength (Δ) as a function of (a) magnon damping (α) for different values of saturation magnetization (M_s), and (b) saturation magnetization (M_s) for different values of magnon damping (α).

the YIG film. For each of the previously studied magnetization values (175 mT, 150 mT, 120 mT, and 90 mT), additional simulations were carried out using two elevated damping values: $\alpha = 1.4 \times 10^{-3}$, and 2.1×10^{-2}. The resulting transmission spectra, displayed in figures S2(a)–(h) of the supplementary material, reveal that the coupling centers resulting from photon–magnon interactions consistently shift toward higher magnetic fields with decreasing M_s, irrespective of the damping level. This trend is consistent with our earlier findings and further confirms the robustness of the theoretical model.

To quantify the effect of damping on coupling strength, the dispersion curves were fitted using equation (9), as indicated by the black solid lines in figures S2(a)–(h). The extracted values of the coupling strength and associated constants for each combination of M_s and α are summarized in table 1. Furthermore, a phase diagram of the coupling constant K as a function of magnetization and damping is presented in figure S3. Theoretical calculations reveal that when the damping parameter of YIG reaches $\alpha_3 = 2.1 \times 10^{-2}$, the system enters the Purcell regime [34, 41], where the radiative decay of the magnon mode dominates over its intrinsic losses. Interestingly, in this regime, we also observed a spontaneous increase in the damping of the hexagonal-ring resonator (HRR), with the damping parameter rising to $\beta = 8.16 \times 10^{-3}$ [42]. While these results are compelling, a detailed analysis of the emergent Purcell effect and the dynamic interplay of dissipation in this regime lies beyond the scope of the present work and will be addressed in a forthcoming publication. However, it should be noted that while intrinsic damping arising from spin–lattice relaxation does not modify the bare coupling strength, extrinsic channels such as Purcell radiation loss become increasingly significant with stronger magnon–photon hybridization [5, 43]. In this work, when we state that changes in dissipation rate or damping modifies the coupling strength, we specifically refer to the combined effect of intrinsic relaxation and extrinsic processes, which together increase the magnon linewidth and thereby reduce cooperativity [30]. As a consequence, enhanced damping suppresses the resolvability of the hybrid modes and diminishes the visibility of mode splitting, consistent with earlier studies in cavity magnonics [27, 39, 44].

To visualize the observed trends, figure 3(a) plots the coupling strength as a function of damping for all the magnetization values, while figure 3(b) presents the variation of coupling strength with saturation magnetization for different YIG damping values. These results clearly indicate that the coupling strength

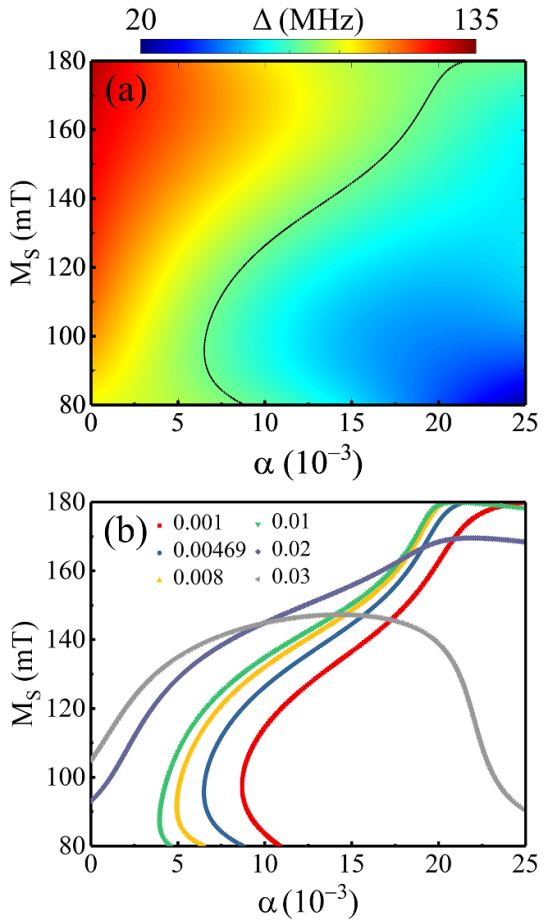

Figure 4. (a) Analytically calculated phase diagram illustrating different types of anti-crossing dispersion on the $(\alpha - M_s)$ plane for an HRR damping value of $\beta = 4.69 \times 10^{-3}$. The color gradient represents the variation in coupling strength (Δ), while the solid black line denotes the contour of constant coupling strength, separating the regions of strong and weak coupling. (b) Contours of constant coupling strength plotted for different values of β, highlighting the effect of HRR damping on the strong–weak coupling boundary.

Table 1. Coupling parameters, coupling strength (Δ) and coupling constant (K), corresponding to different values of saturation magnetization (M_s).

	Coupling strength (MHz)			Coupling constant (K)		
M_S (mT)	$\alpha_1 = 1.4 \times 10^{-5}$	$\alpha_2 = 1.4 \times 10^{-3}$	$\alpha_3 = 2.1 \times 10^{-2}$	$\alpha_1 = 1.4 \times 10^{-5}$	$\alpha_2 = 1.4 \times 10^{-3}$	$\alpha_3 = 2.1 \times 10^{-2}$
90	97.68	92.88	51.93	0.038	0.036	0.024
120	113	105.86	63.14	0.038	0.0355	0.024
150	121.4	116.76	72.63	0.0365	0.035	0.024
175	127.6	122.55	79.6	0.0355	0.034	0.024

in PMC systems decreases both with increasing damping and with decreasing saturation magnetization. This underscores the importance of optimizing both magnetic order and damping characteristics in magnonic materials to achieve and maintain strong PMC.

To gain deeper insights into the interdependence of the α and M_s on the PMC strength Δ, we constructed a phase diagram of the anticrossing behavior in the $\alpha - M_s$ parameter space. This diagram, shown in figure 4(a), was generated using equation (10), with the coupling constant K values taken from table 1, the resonator damping parameter fixed at $\beta = 4.69 \times 10^{-3}$, and $\omega_c/2\pi = 5.33$ GHz. In the phase diagram, the black solid line outlines a contour of constant coupling strength, separating regions of varying Δ. The color gradient visualizes the variation in Δ across the $\alpha - M_s$ plane: darker red tones signify stronger coupling, while dark blue tones indicate weaker coupling. As expected from theory and simulations, the coupling strength increases with increasing saturation magnetization and decreases with increasing magnon damping. This is consistent with the relation $\Delta \propto \sqrt{M_s}$ and the known detrimental effect of damping on coherent coupling. The dark blue region, located at the intersection of high

damping and low magnetization, corresponds to the weakest coupling regime. In contrast, the dark red region characterized by low damping and high magnetization marks the strongest coupling regime.

To generalize this behavior for varying resonator damping, figure 4(b) shows contours of constant coupling strength for different values of β (such as 0.001, 0.00469, 0.008, 0.01, 0.02, 0.03), with their corresponding colormap representations provided in figure S4 of the supplementary material. These additional plots illustrate how changes in the HRR's intrinsic damping influence the coupling landscape. As β increases, the contours shift downward in the α axis, indicating that higher HRR damping leads to a reduction in the effective coupling strength at a given magnetization. Interestingly, for larger values of β, the upper segment of the contour begins to bend rightward toward higher α and intersects with the upper portion of the previous contour. This behavior becomes particularly prominent for $\beta = 0.03$, where the contour undergoes a significant shape deformation (also highlighted in figure S4(g)). In this regime, where the magnon damping is high and magnetization is low, the contour reveals an unexpected result: stronger coupling can still be achieved if the photon mode is embedded in a resonator with sufficiently high intrinsic damping. This suggests a non-trivial interplay between the dissipative properties of both subsystems, hinting at the possibility of entering non-Hermitian or Purcell-like coupling regimes. These findings demonstrate that the coupling strength in PMC systems can be flexibly tuned not only through intrinsic material parameters such as M_s and α but also via the deliberate engineering of resonator losses β. This multidimensional tuning capability offers a powerful strategy for tailoring hybrid system dynamics. Furthermore, it is worth highlighting that compared with conventional methods, our M_s-based tuning provides clear advantages. Geometry modification can enhance coupling but is permanent and requires re-fabrication, while magnetic bias mainly shifts resonance frequencies rather than directly tuning the coupling. In contrast, varying M_s offers reversible, in-situ control within the same device, without altering geometry or external bias fields. Notably, while earlier studies reported up to 50%–64% enhancement through resonator reshaping or magnetic field adjustment [45, 46], our HRR–YIG system demonstrates nearly a 150% increase in coupling strength, establishing M_s tuning as a more versatile and powerful approach.

In practical terms, magnetization and damping can be controlled through several well-established methods. The M_s is highly sensitive to factors such as temperature, chemical composition, and structural order. For example, increasing the temperature reduces magnetic order and thus lowers M_s, as predicted by Bloch's law for ferromagnets [35]. Since the collective PMC strength scales as $\Delta \propto \sqrt{N} \propto \sqrt{M_S}$, where N is the effective number of spins contributing to the interaction, a temperature-induced reduction in M_s weakens the coupling strength, while lower temperatures enhance it. Near room temperature, this dependence is captured by Bloch's law: $M_S(T) = M_S(0)\left[1-(T/T_C)^{3/2}\right]$, where T_C is the Curie temperature. Accordingly, the coupling strength follows $\Delta \propto \sqrt{M_S(T)}$, highlighting the direct role of thermal effects in modulating photon–magnon interactions in YIG-based hybrid systems. Similarly, introducing non-magnetic dopants or changing stoichiometry in YIG films (e.g. substituting Fe with Ga or Al) can reduce the net spin density, thereby tuning M_s [47]. On the other hand, the Gilbert damping parameter can be engineered through interface engineering, impurity doping, or varying film thickness. For instance, increasing surface roughness or introducing rare-earth impurities in YIG (e.g. Tb, Dy) has been shown to significantly enhance α by increasing spin-lattice relaxation and magnon-phonon scattering [47, 48]. Furthermore, deposition techniques such as pulsed laser deposition and liquid-phase epitaxy allow precise control over film crystallinity and defect density, thereby offering pathways to tailor both M_s and α [49–51]. Therefore, this approach not only provides a new degree of freedom in coupling control but also enables access to previously unexplored regimes of hybrid interactions, such as enhanced non-Hermitian dynamics [52], tunable exceptional surfaces [18, 53], and expanded nonreciprocal bandwidths [54]. Harnessing magnetization-based tuning along with individual damping control of magnons and photons could significantly advance PMC research. It holds particular promise for the development of reconfigurable, chip-scale HQSs, where achieving an optimal balance between coherent interaction strength and dissipation is crucial. Such control is vital for next-generation applications in quantum transduction, information storage, and on-chip coherent sensing.

4. Conclusion

In conclusion, we present a novel method to tune the coupling strength in photon–magnon hybrid systems by manipulating the magnetic properties of the magnonic material, specifically saturation magnetization M_s, damping α, or a combination of both. Our results demonstrate that the coupling strength of HRR–YIG hybridized modes can be effectively controlled through the M_s of YIG. A decrease in M_s or an increase in α leads to a noticeable reduction in coupling strength. These findings are validated using an

electrodynamic model, which shows good agreement with simulation results. Furthermore, we propose a generalized framework for tailoring the coupling strength across a wide range of system parameters. Looking forward, experimental validation through controlled tuning of M_s via temperature, strain, or material engineering will be an essential step toward practical implementation. The ability to dynamically regulate coupling strength is particularly promising for quantum memories, non-reciprocal microwave devices, and coherent signal transduction. Such advances will establish M_s-tuning as a versatile tool for engineering next-generation hybrid quantum devices, where robust and reconfigurable photon–magnon interactions are critical for quantum information processing and related technologies.

Data availability statement

All data that support the findings of this study are included within the article (and any supplementary files).

Acknowledgments

The work was supported by the Council of Science and Technology, Uttar Pradesh (CSTUP), (Project Id: 2470, CST, U.P. Sanction No: CST/D-1520). B Bhoi acknowledges support by the Science and Engineering Research Board (SERB) India- SRG/2023/001355. R Singh acknowledges support from the Council of Science and Technology, Uttar Pradesh (CSTUP), (Project Id: 4482). S Verma acknowledges the Ministry of Education, Government of India, for the Prime Minister's Research Fellowship (PMRF ID-1102628).

ORCID iD

Biswanath Bhoi 0000-0002-1405-8196

References

[1] Zhang X 2023 A review of common materials for hybrid quantum magnonics *Mater. Today Electron.* **5** 100044
[2] Li Y, Zhang W, Tyberkevych V, Kwok W-K, Hoffmann A and Novosad V 2020 Hybrid magnonics: physics, circuits and applications for coherent information processing *J. Appl. Phys.* **128** 130902
[3] Xiang Z-L, Ashhab S, You J and Nori F 2013 Hybrid quantum circuits: superconducting circuits interacting with other quantum systems *Rev. Mod. Phys.* **85** 623
[4] Kurizki G, Bertet P, Kubo Y, Mølmer K, Petrosyan D, Rabl P and Schmiedmayer J 2015 Quantum technologies with hybrid systems *Proc. Natl Acad. Sci.* **112** 3866
[5] Lachance-Quirion D, Tabuchi Y, Gloppe A, Usami K and Nakamura Y 2019 Hybrid quantum systems based on magnonics *Appl. Phys. Express* **12** 070101
[6] Yuan H, Cao Y, Kamra A, Duine R A and Yan P 2022 Quantum magnonics: when magnon spintronics meets quantum information science *Phys. Rep.* **965** 1
[7] Kantsepolsky B, Aviv I, Weitzfeld R and Bordo E 2023 Exploring quantum sensing potential for systems applications *IEEE Access* **11** 31569
[8] Degen C L, Reinhard F and Cappellaro P 2017 Quantum sensing *Rev. Mod. Phys.* **89** 035002
[9] Wang C-H, Li F and Jiang L 2022 Quantum capacities of transducers *Nat. Commun.* **13** 6698
[10] Heshami K, England D G, Humphreys P C, Bustard P J, Acosta V M, Nunn J and Sussman B J 2016 Quantum memories: emerging applications and recent advances *J. Mod. Opt.* **63** 2005
[11] Nielsen M A and Chuang I L 2010 *Quantum Computation and Quantum Information* (Cambridge University Press)
[12] Yang Y, Rao J, Gui Y, Yao B, Lu W and Hu C-M 2019 Control of the magnon-photon level attraction in a planar cavity *Phys. Rev. Appl.* **11** 054023
[13] Wang Y-P, Rao J, Yang Y, Xu P-C, Gui Y, Yao B, You J and Hu C-M 2019 Nonreciprocity and unidirectional invisibility in cavity magnonics *Phys. Rev. Lett.* **123** 127202
[14] El-Ganainy R, Makris K G, Khajavikhan M, Musslimani Z H, Rotter S and Christodoulides D N 2018 Non-Hermitian physics and PT symmetry *Nat. Phys.* **14** 11
[15] Ashida Y, Gong Z and Ueda M 2020 Non-Hermitian physics *Adv. Phys.* **69** 249
[16] Miri M-A and Alu A 2019 Exceptional points in optics and photonics *Science* **363** eaar7709
[17] Özdemir Ş K, Rotter S, Nori F and Yang L 2019 Parity–time symmetry and exceptional points in photonics *Nat. Mater.* **18** 783
[18] Cerjan A 2019 A whole surface of exceptional points *Physics* **12** 138
[19] Wagle D, Rai A, Kaffash M T and Jungfleisch M B 2024 Controlling magnon-photon coupling in a planar geometry *J. Phys. Mater.* **7** 025005
[20] McKenzie-Sell L, Xie J, Lee C-M, Robinson J W, Ciccarelli C and Haigh J A 2019 Low-impedance superconducting microwave resonators for strong coupling to small magnetic mode volumes *Phys. Rev. B* **99** 140414
[21] Rao J, Wang C, Yao B, Chen Z, Zhao K and Lu W 2023 Meterscale strong coupling between magnons and photons *Phys. Rev. Lett.* **131** 106702
[22] Maurya A, Shrivastava K K, Verma S, Singh R and Bhoi B 2024 Room temperature photon-magnon coupling in YIG-electric field coupled resonator system *Chem. Phys. Impact* **9** 100669
[23] Verma S, Maurya A, Singh R and Bhoi B 2024 Control of photon-magnon coupling in a planar hybrid configuration *J. Supercond. Nov. Magn.* **37** 1163

[24] Samanta S, Pradhan R and Syam D 2021 Theoretical approach to verify the resonance frequency of a square split ring resonator *J. Opt. Soc. Am. B* **38** 2887
[25] Kaur H J and Goyal P 2021 Comparison of two loop photonic crystal: ring-resonator with hexagonal and rectangular lattice structure *J. Opt.* **50** 223
[26] Silva T J, Lee C, Crawford T and Rogers C T 1999 Inductive measurement of ultrafast magnetization dynamics in thin-film permalloy *J. Appl. Phys.* **85** 7849
[27] Bai L, Harder M, Chen Y, Fan X, Xiao J and Hu C-M 2015 Spin pumping in electrodynamically coupled magnon-photon systems *Phys. Rev. Lett.* **114** 227201
[28] Bhoi B, Kim B, Jang S-H, Kim J, Yang J, Cho Y-J and Kim S-K 2019 Abnormal anticrossing effect in photon-magnon coupling *Phys. Rev. B* **99** 134426
[29] Grigoryan V L and Xia K 2019 Cavity-mediated dissipative spin-spin coupling *Phys. Rev. B* **100** 014415
[30] Harder M, Bai L, Match C, Sirker J and Hu C 2016 Study of the cavity-magnon-polariton transmission line shape *Sci. China Phys., Mech. Astron.* **59** 1
[31] Grigoryan V L, Shen K and Xia K 2018 Synchronized spin-photon coupling in a microwave cavity *Phys. Rev. B* **98** 024406
[32] Bloembergen N and Pershan P 1962 Light waves at the boundary of nonlinear media *Phys. Rev.* **128** 606
[33] Grigoryan V L and Xia K 2019 Thermally induced monochromatic microwave generation in magnon polaritons *Phys. Rev. B* **99** 224408
[34] Zhang X, Zou C-L, Jiang L and Tang H X 2014 Strongly coupled magnons and cavity microwave photons *Phys. Rev. Lett.* **113** 156401
[35] Kittel C and McEuen P 2018 *Introduction to Solid State Physics* (Wiley)
[36] Blundell S 2001 *Magnetism in Condensed Matter* (OUP Oxford)
[37] Rao J, Wang Y, Yang Y, Yu T, Gui Y, Fan X, Xue D and Hu C-M 2020 Interactions between a magnon mode and a cavity photon mode mediated by traveling photons *Phys. Rev. B* **101** 064404
[38] Bhoi B and Kim S-K 2019 Photon-magnon coupling: historical perspective, status and future directions *Solid State Phys.* **70** 1
[39] Huebl H, Zollitsch C W, Lotze J, Hocke F, Greifenstein M, Marx A, Gross R and Goennenwein S T 2013 High cooperativity in coupled microwave resonator ferrimagnetic insulator hybrids *Phys. Rev. Lett.* **111** 127003
[40] Harder M, Yang Y, Yao B, Yu C, Rao J, Gui Y, Stamps R and Hu C-M 2018 Level attraction due to dissipative magnon-photon coupling *Phys. Rev. Lett.* **121** 137203
[41] Zhao Y, Wang L, Han X, Tian Y, Yan S, Guo Q, Zhai Y and Bai L 2023 Control of magnon–photon coupling by a direct current in a py/pt-superconducting cavity hybrid system *Appl. Phys. Lett.* **122** 222403
[42] Verma S, Maurya A, Khan F, Srivastava K K, Singh R and Bhoi B 2025 Hybrid photon-magnon systems: exploring the purcell effect (arXiv:2501.04574)
[43] Zhang X, Zou C-L, Zhu N, Marquardt F, Jiang L and Tang H X 2015 Magnon dark modes and gradient memory *Nat. Commun.* **6** 8914
[44] Tabuchi Y, Ishino S, Noguchi A, Ishikawa T, Yamazaki R, Usami K and Nakamura Y 2015 Coherent coupling between a ferromagnetic magnon and a superconducting qubit *Science* **349** 405
[45] Girich A, Nedukh S, Polevoy S, Sova K, Tarapov S and Vakula A 2023 Enhancement of the microwave photon-magnon coupling strength for a planar fabricated resonator *Sci. Rep.* **13** 924
[46] Bhoi B, Kim B, Kim J, Cho Y-J and Kim S-K 2017 Robust magnon-photon coupling in a planar-geometry hybrid of inverted split-ring resonator and YIG film *Sci. Rep.* **7** 11930
[47] Sharma V and Kuanr B K 2018 Magnetic and crystallographic properties of rare-earth substituted yttrium-iron garnet *J. Alloys Compd.* **748** 591
[48] Bhoi B, Kim B, Kim Y, Kim M-K, Lee J-H and Kim S-K 2018 Stress-induced magnetic properties of pld-grown high-quality ultrathin YIG films *J. Appl. Phys.* **123** 203902
[49] Bhoi B, Venkataramani N, Aiyar R and Prasad S 2013 FMR and magnetic studies on polycrystalline YIG thin films deposited using pulsed laser *IEEE Trans. Magn.* **49** 990
[50] Will-Cole A *et al* 2023 Negligible magnetic losses at low temperatures in liquid phase epitaxy grown $Y_3Fe_5O_{12}$ films *Phys. Rev. Mater.* **7** 054411
[51] Sun Y *et al* 2013 Damping in yttrium iron garnet nanoscale films capped by platinum *Phys. Rev. Lett.* **111** 106601
[52] Wang Y-X and Clerk A 2019 Non-Hermitian dynamics without dissipation in quantum systems *Phys. Rev. A* **99** 063834
[53] Ergoktas M S *et al* 2022 Topological engineering of terahertz light using electrically tunable exceptional point singularities *Science* **376** 184
[54] Mann S A, Sounas D L and Alu A 2019 Nonreciprocal cavities and the time–bandwidth limit *Optica* **6** 104
[55] Xu H, Mason D, Jiang L and Harris J 2016 Topological energy transfer in an optomechanical system with exceptional points *Nature* **537** 80